Separation and Purification Technology 250 (2020) 117237

Contents lists available at ScienceDirect

Separation and Purification Technology

journal homepage: www.elsevier.com/locate/seppur

Peroxymonosulfate activation of magnetic Co nanoparticles relative to an N-doped porous carbon under confinement: Boosting stability and performance

Jiao Cao[a,b], Zhaohui Yang[a,b,*], Weiping Xiong[a,b,*], Yaoyu Zhou[c], You Wu[a,b], Meiying Jia[a,b], Saiwu Sun[a,b], Chengyun Zhou[a,b], Yanru Zhang[a,b], Renhua Zhong[d]

[a] College of Environmental Science and Engineering, Hunan University, Changsha 410082, PR China
[b] Key Laboratory of Environmental Biology and Pollution Control (Hunan University), Ministry of Education, Changsha 410082, PR China
[c] College of Resources and Environment, Hunan Agricultural University, Changsha 410128, PR China
[d] Hunan Yaoheng Environmental Technology Co Ltd, Changsha 410200, PR China

ARTICLE INFO

Keywords:
Zeolitic imidazolate frameworks (ZIF-67)
Co nanoparticles
peroxymonosulfate (PMS)
Confinement

ABSTRACT

The integration of metal nanoparticles into carbon materials has catch considerable attention. In this study, we have successfully fabricated the N-doped porous carbon encapsulated magnetic Co nanoparticles (Co@NC-800) through a two-step pyrosis of zeolitic imidazolate frameworks (ZIF-67). The obtained Co@NC-800 exhibited excellent stability in activating peroxymonosulfate (PMS) towards tetracycline (TC) degradation without obvious Co leaching and magnetically separable. The removal efficiency reached up to 90.1% within 3 min and 74.7% of total organic carbon (TOC) removal efficiency could be obtained in 30 min towards TC by Co@NC-800/PMS system. Mechanism explorations revealed the encapsulated Co nanoparticles in the porous N-doped carbon promoted the catalytic activity and stability. The two-pathway mechanism study indicated that radical and non-radical oxidations acted together in TC degradation. Moreover, some potential factors, including PMS dosage, TC concentration, solution pH value, anion/organic matters and temperature were investigated. The Co@NC-800/PMS system exhibited high efficiency in removal of various antibiotics (oxytetracycline, chlortetracycline and deoxytetracycline). Even in actual water bodies (tap water, river water and pharmaceutical wastewater), the Co@NC-800/PMS system displayed excellent performance. This study proposed a design of metal nanoparticles under confinement for fabricating highly active catalysts towards PMS activation.

1. Introduction

In recent decades, high production and consumption of pharmaceutical and personal care products (PPCPs) are bringing threats to the aquatic environment and human health [1–6]. Advanced oxidation processes (AOPs) referring to the production of reactive oxygen species (ROS) showed the superiority for organics removal due to its high mineralization and easy operation [7–12]. Peroxymonosulfate (PMS) is a typical oxidant that various methods like irradiation, heating, ultrasound and transition metal catalysis can be applied to activate PMS to generate ROS for wastewater remediation [13]. Previous researches are generally focused on the generation of radicals like sulfate radical ($SO_4^{\cdot -}$), hydroxyl radical ($^{\cdot}OH$ radical) and superoxide radical ($O_2^{\cdot -}$), while ignoring non-radical like singlet oxygen ($^1O_2$) [14]. Due to the high reaction rate ($\approx 2 \times 108\ m^{-1}\ S^{-1}$) and low activation energy (7.4 ± 2.4 kcal mol^{-1}), the self-decompose of PMS can occur and produce $^1O_2$ [13,15]. $^1O_2$ induced oxidation reaction possess a relatively high catalytic performance and suffer less interference from water bodies compared to $SO_4^{\cdot -}$, $^{\cdot}OH$ and $O_2^{\cdot -}$ radicals [16].

The AOPs of metal nanoparticles under confinement has generated new insights in the field of environmental remediation. The confinement strategy of carbon-encapsulated materials exhibited significant advantages in catalytic reactions due to their unique heterostructures and electronic configuration [17]. For example, Pan's group reported the Fenton reaction by Fe_2O_3 confined in carbon nanotube (Fe_2O_3@CNT-H) catalyst and found that the catalyst using nanoconfinement for organics removal exhibited extremely high activity and pH suitability [18]. The high activity and enhanced stability of catalysts can be achieved via confined strategy [19]. Liu et al. [20] fabricated N-doped graphitic carbon nanotubes encapsulated FeCo nanoparticles and

* Corresponding authors at: College of Environmental Science and Engineering, Hunan University, Changsha, Hunan 410082, PR China.
E-mail addresses: yzh@hnu.edu.cn (Z. Yang), xiongweiping@hnu.edu.cn (W. Xiong).

https://doi.org/10.1016/j.seppur.2020.117237
Received 3 May 2020; Received in revised form 4 June 2020; Accepted 7 June 2020
Available online 10 June 2020

found that the existence of strong synergetic coupling promoted the catalytic activity. Lei's group found that Co confined in graphitic-N-doped nanotube was more active than Co confined in pyridinic-N-doped nanotube [21]. Therefore, the metal-support interaction played essential role in the catalytic performance [22,23].

Metal-organic frameworks (MOFs) possess three-dimensional and well-ordered structure, enabling it an ideal platform for the fabrication of metal NPs confined in porous carbon by pyrolysis method [24]. During the pyrolysis process in inert gases, the organic linkers in MOFs were transformed into carbon framework and the metal NPs gradually formed. The metal NPs could induce the graphitization of carbon and be confined within the graphite carbon [25]. Chen et al. [26] employed Prussian blue analogue ($Co_3[Fe(CN)_6]_2$) for fabricating a magnetic carbon/cobalt/iron composite via a one-step pyrolysis method. The obtained magnetic carbon/cobalt/iron composite composed of uniformly-distributed cobalt and cobalt ferrite confined in a porous carbon substrate and exhibited activity for activating peroxymonosulfate (PMS) to degrade Rhodamine B (RhB). Researches indicated the presence of N species within the carbon would remarkably increase the density of states near the Fermi level and accelerate the electron between the inner metal and outer carbon shell, which made for the catalytic reaction [27]. Song et al. [28] fabricated Fe/Fe_3C@N-doped porous carbon by pyrolyzing of Fe-MIL-88B-NH_2 and estimated the catalytic performance by activating PMS to degrade 4-chlorophenol (4-CP) from aqueous solution. The efficient electron transfer between Fe NPs and the N heteroatom conduced to the high performance.

As a subclass of MOFs, zeolitic imidazolate frameworks (ZIFs) with abundant and ordered N species would be an ideal precursor to synthesize metal nanoparticles confined in N-doped carbon [29]. The combination of ZIFs-based confinement strategy and AOPs is probably a potential strategy to remove the organic contaminant with high efficiency. Co-based ZIFs (ZIF-67) with rhombic dodecahedron morphology have been widely studied to synthesis metal and N co-doped carbon materials (M-N-C) for its abundant Co and N species [30,31]. The obtained M-N-C inherited the porous property of pristine ZIF-67 and the M-N-C bond can bring out active sites for catalytic reaction. Furthermore, Co-based catalyst usually shows magnetism, which can be magnetically separated after catalytic runs.

With these things in mind, ZIF-67 was selected as self-sacrificial template and pyrolyzed at two stages under nitrogen atmosphere to obtain N-doped porous carbon encapsulated Co nanoparticles (Co@NC-800). Two-step pyrolysis method can maximize the maintenance of the porous structure of the pristine ZIF-67 in contrast to the direct pyrolysis process. As a kind of typical, tetracycline (TC) was chosen as the target contaminant. The obtained Co@NC-800 exhibited high catalytic activity in TC degradation via the activation of PMS. The morphology, crystalline phase, composition, pore structure and electrochemical property of catalysts were characterized. Moreover, the catalytic mechanism based on electrochemical characterizations, X-ray photoelectron spectroscopy (XPS) analysis, tripping experiments and Electron Paramagnetic Resonance (EPR) results were proposed. In addition, the Co leaching and recycling experiments were taken into account to evaluate the stability of catalyst. Multiple antibiotics (oxytetracycline, chlortetracycline and deoxytetracycline) and various water bodies (tap water, river water and pharmaceutical wastewater) were applied to estimate the practical application potential of Co@NC-800 catalyst. This study presented the superiority of fabricating catalyst under confinement and provided a versatile method to design catalyst with high efficiency in wastewater remediation.

2. Materials and method

2.1. Materials preparation

Synthesis of ZIF-67: $Co(NO_3)_2{\cdot}6H_2O$ (5 mmol, 1.4551 g) and 2-methylimidazole (20 mmol, 1.642 g) were dissolved in 50 mL of methanol, respectively. Then, the 2-methylimidazole solution was slowly added into $Co(NO_3)_2{\cdot}6H_2O$ solution and continuously stirred for 20 h at room temperature. The obtained purple products were collected and centrifugal washed by methanol for three times. Finally, the ZIF-67 powder was harvested after vacuum dried at 60 ˚C overnight.

Synthesis of Co@NC-800: A certain amount of ZIF-67 was placed into a quartz boat and put into the middle of the quartz tube. After nitrogen was inlet for 1 h, the furnace was heated was heated from room temperature to 300 ˚C for 1 h with a heating rate of 5 ˚C/min. Afterward, the furnace was then heated into 800 ˚C with a heating rate of 5 ˚C/min and kept for 2 h. The sample was naturally cooled down to room temperature. The resultant products were washed with deionized water and magnetic collected and then vacuum dried at 60 ˚C overnight.

Synthesis of NC-800: The obtained Co@NC-800 was immersed in HF (20% vol) solution for 24 h to remove the Co nanoparticles. Finally, the black powders were collected and centrifugal washed by deionized water for three times and vacuum dried overnight.

2.2. Experiments method

The degradation experiments were conducted in 250 mL beakers containing 100 mL of 30 mg L^{-1} TC solution. 20 mg of samples were added into TC solution with continuously magnetic stirring for 60 min to reach adsorption equilibrium. The TC concentration after adsorption equilibrium was applied as the zero point. Then, 20 mg of PMS were added and stirred for 30 min. Samples were collected and measured after a regular time interval. If not specified, the pH value of TC solution used in the experiment was unadjusted.

3. Results and discussion

3.1. Structure characterization

The preparation process of the Co@NC-800 was illustrated in Fig. 1a. As Fig. 1a and b displayed, the ZIF-67 crystal presented a uniform rhombic dodecahedral morphology with an average size of 600 nm. Moreover, X-ray powder diffraction (XRD) patterns (Fig. 2a) of the as-synthesized ZIF-67 fitted well with the simulated data of ZIF-67, representing the ZIF-67 crystals were successful synthesized [32–34]. The obtained Co@NC-800 inherited rhombic dodecahedron morphology and the particle size was almost unchanged, while the surface of Co@NC-800 was much rougher (Fig. 1d and e). The XRD patterns of Co@NC-800 (Fig. 2b) exhibited three sharp peaks belonged to metallic Co (PDF#15-0806) at $2\theta = 44.216$ (1 1 1), 51.522 (2 0 0) and 75.853 (2 2 0), demonstrating the presence of Co nanoparticles [35]. During the pyrolysis process, the organic linkers of ZIF-67 were transformed into an N-doped carbon skeleton and the surface of ZIF-67 started to shrink. Subsequently, the Co nanoparticles gradually formed [25]. After the pyrolysis process, the magnetic powder (Co@NC-800) was washed thoroughly with HF solution (20% vol) to remove the existing Co nanoparticles. The morphology of NC-800 was consistent with the Co@NC-800 (Fig. 1f and g). The characteristic peaks of metallic Co in NC-800 XRD pattern almost disappeared (Fig. S1), indicating the acid treatment by HF could remove the Co cores [25].

Transmission electron microscopy (TEM) analysis confirmed the rhombic dodecahedral morphology of Co@NC-800 (Fig. 1h and i) and the metallic Co nanoparticles uniformly distributed with the particle size of 5–20 nm. Moreover, the high-resolution transmission electron microscopy (HRTEM) image (Fig. 1n) showed that Co nanoparticles were confined in the carbon layers derived from the carbonization of the 2-methylimidazole ligand in ZIF-67 [36] and the well-defined interplanar distance about 0.20 nm in accordance with the (1 1 1) lattice plane of metallic Co, which confirmed the XRD results. The selected area electron diffraction (SAED) pattern showed individual rings which belonged to the (1 1 1), (2 0 0), (2 2 0) and (3 1 1) facets of metallic Co

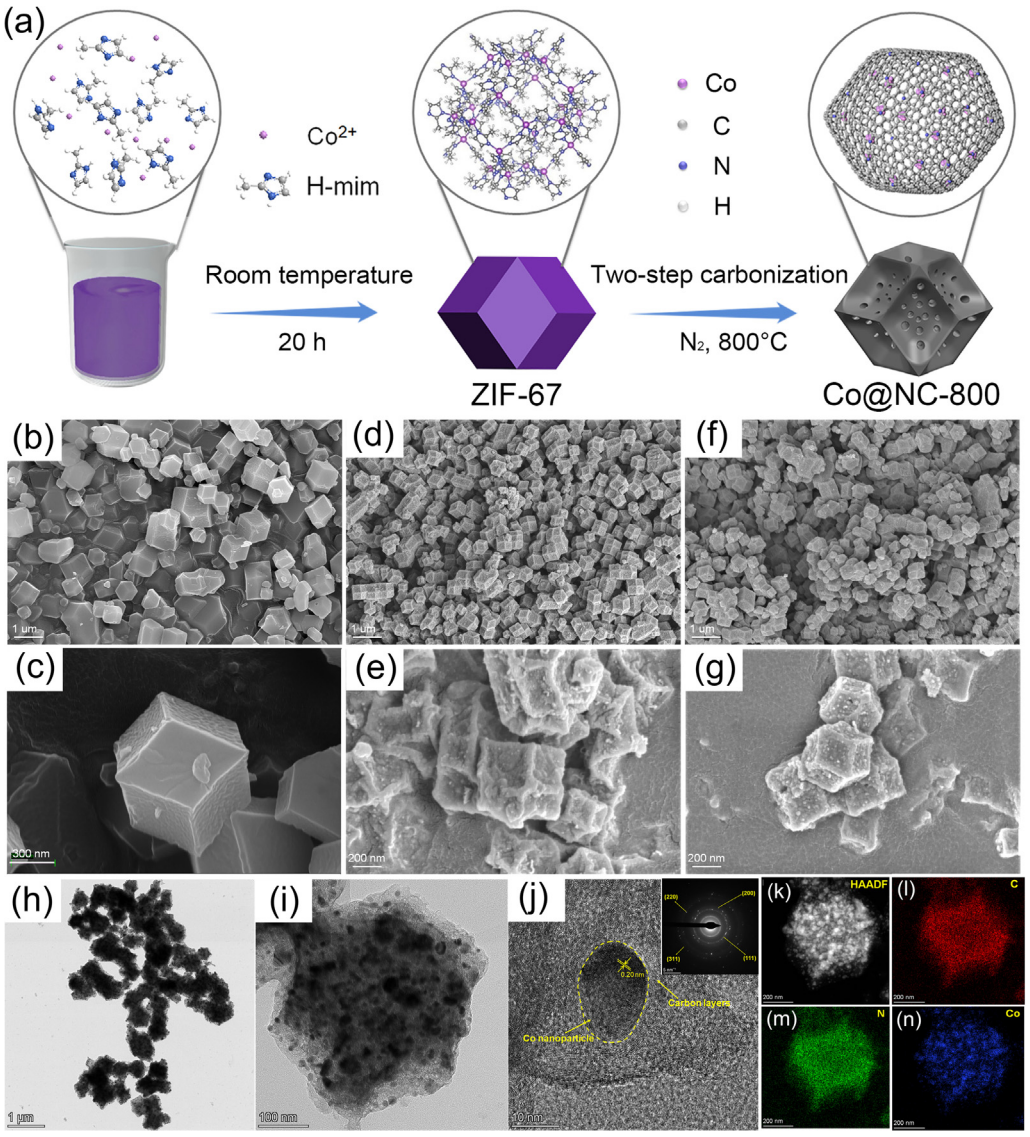

Fig. 1. (a) Schematic illustration of the preparation procedure of Co@NC-800; SEM images of ZIF-67 (b and c), Co@NC-800 (d and e) and NC-800 (f and g); (h and i) TEM images of Co@NC-800; (j) HAADF-TEM image of Co@NC-800 and corresponding elemental mappings of (k) C, (l) N and (m) Co elements; (n) HRTEM image of Co@NC-800 (the insert figure was the SAED pattern).

(Fig. 1n, inserted). Elemental mapping under TEM mode (Fig. 1j–m) showed the homogeneous distribution of C, N, and Co elements throughout the Co@NC-800.

XPS survey spectra verified the existence of C, N and Co elements on the surface of ZIF-67 and Co@NC-800 (Fig. 3a). Compared to the pristine ZIF-67, the N content in Co@NC-800 decreased while the C content increased. The Co 2p spectra (Fig. 3b) showed four distinct peaks of Co^{3+}-O/N, Co^{2+}-O/N, Co^{0} and satellite peak, the content of

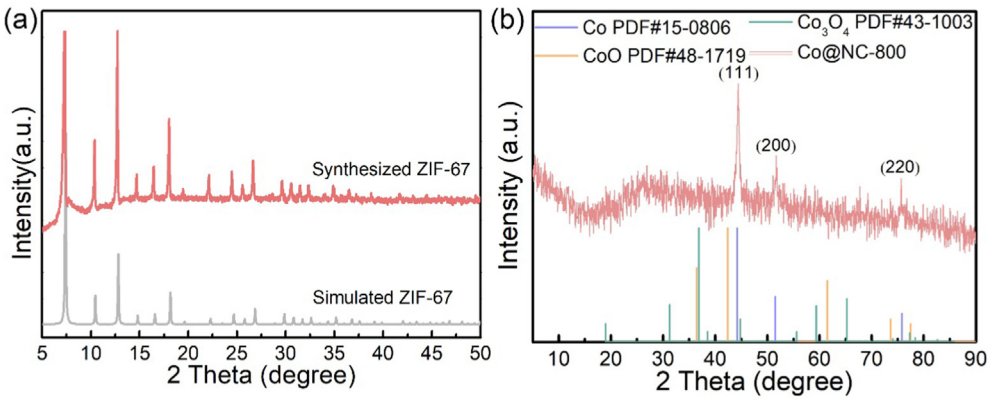

Fig. 2. Powder XRD patterns of ZIF-67 and simulated ZIF-67 (a) and Co@NC-800 (b).

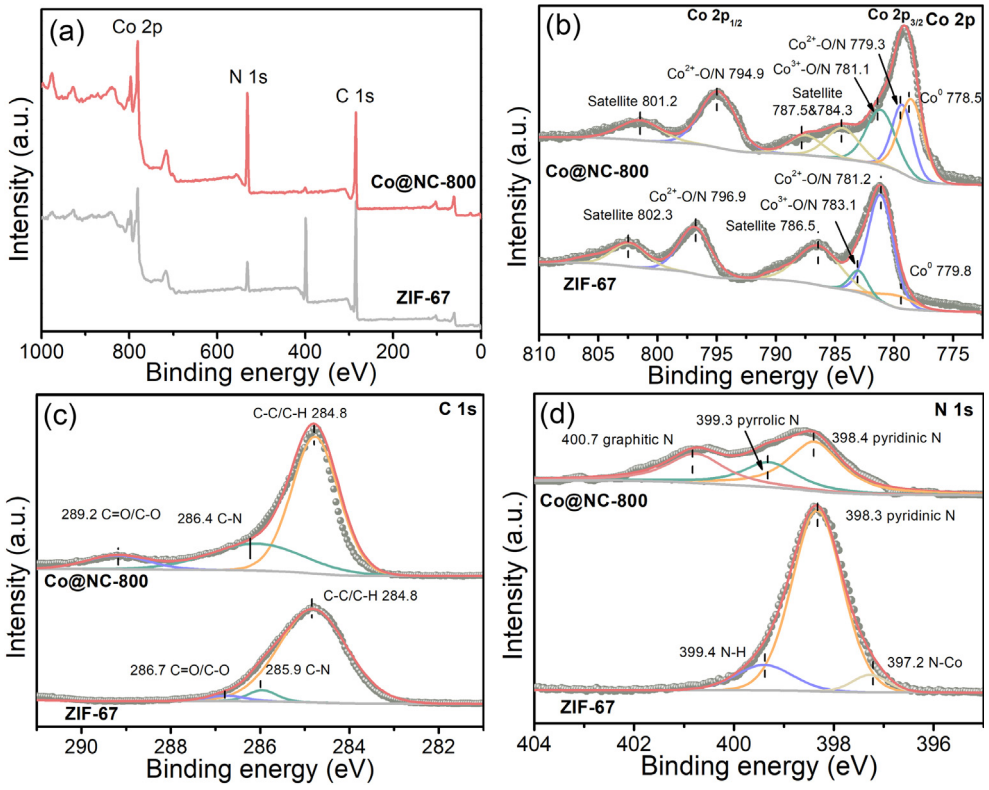

Fig. 3. XPS spectra of ZIF-67 and Co@NC-800: (a) survey; (b) Co 2p; (c) C 1s and (d) N 1s.

Co^0 species in Co@NC-800 increased obviously compared to ZIF-67, verified the XRD and TEM results. The Co nanoparticles could bond to the adjacent N or O atoms to form Co-N or Co-O bonds and brought out more catalytic active sites [37]. It can be observed that the Co 2p peak components shifted into lower binding energy, suggesting that the electron density on Co increased and the average electronic state of Co shifted to the lower valence [38]. Moreover, the C 1s and N 1s peaks moved to higher binding energy, indicating that electron transfer occurred between Co, C and N atoms [39,40]. Additionally, the graphitic N content increased obviously, thermal-instability pyridinic N tended to transform into graphitic N [41]. The above results suggested that the carbonization of ZIF-67 resulted in Co nanoparticles confined in the N-doped porous carbon. Moreover, the inductively coupled plasma optical emission spectrometer (ICP-OES) analysis quantified the Co content in Co@NC-800 was 19.46%.

Nitrogen adsorption-desorption isotherm (Fig. 4a) indicated when the $p/p_0 < 0.2$, the adsorbed quantity within ZIF-67, NC-800 and Co@NC-800 samples increased rapidly, suggesting the presence of micropores. However, when $p/p_0 > 0.2$, the adsorbed quantity of the above samples increased slowly while there was a hysteresis loop in the adsorption isotherm of NC-800, indicating the existence of mesopores. The nitrogen sorption results showed the typical type I isotherm for ZIF-67 and Co@NC-800, matching its microporous character and the pore size was mainly distributed in the range of 0–5 nm. Moreover, the nitrogen adsorption isotherm of NC-800 was analogous to type-IV, and the pore size of NC-800 mainly fall into the range of 3–5 nm with some larger ones between 10 and 30 nm. The Brunauer-Emmett-Teller (BET) surface area of ZIF-67, NC-800 and Co@NC-800 were 2169.78 $m^2\ g^{-1}$, 453.22 $m^2\ g^{-1}$ and 335.52 $m^2\ g^{-1}$, respectively. The pore size and pore volume of the samples were presented in Table 1. Compared to the pristine ZIF-67, the pore size of NC-800 and Co@NC-800 increased while the pore volume decreased. During the pyrolysis process, the ZIF-67 surface started to shrink and the Co fell off. With HF treatment, the obtained NC-800 possessed both micropores and mesopores. The

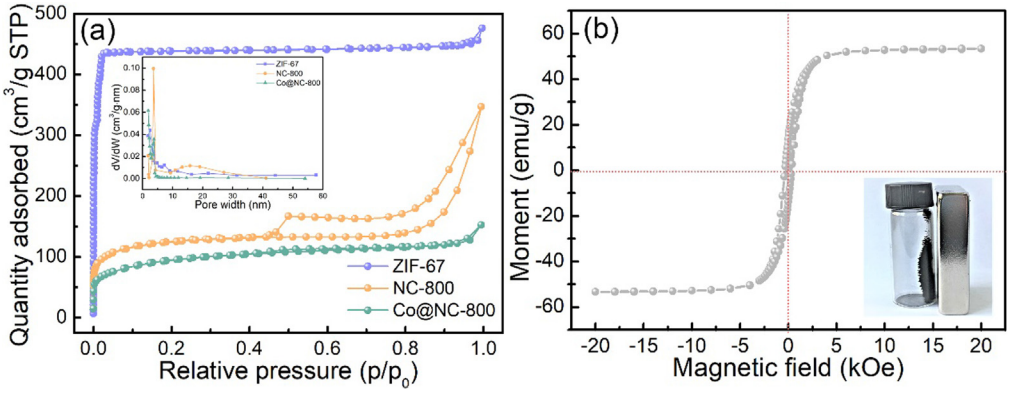

Fig. 4. (a) Nitrogen adsorption and desorption isotherms for ZIF-8, NC-800 and Co@NC-800 (pore size distributions inserted); (b) room-temperature magnetization curve of Co@NC-800.

Table 1
Surface area, pore size and pore volume parameters of ZIF-67, NC-800 and Co@NC-800.

Samples	Surface area[a] (m^2g^{-1})	Pore size[b] (nm)	Pore volume[c] (cm^3g^{-1})
ZIF-67	2169.78	3.80	0.74
NC-800	453.22	12.20	0.54
Co@NC-800	335.52	4.71	0.24

[a] Measured using N_2 adsorption with the Brunauer–Emmett–Teller (BET) method.
[b] Pore size in diameter calculated by the desorption data using Barrett–Joyner–Halenda (BJH) method.
[c] Total pore volume determined at $P/P_0 = 0.99$.

microporous structure inherited from the pristine ZIF-67 while the mesopores were due to the removal of Co nanoparticles. The porous structure of the obtained Co@NC-800 was conductive to pollutants diffusion and active sites exposition [42]. In addition, the magnetic property of Co@NC-800 was tested by VSM system at room temperature (Fig. 4b). The magnetization saturation values (Ms) of Co@NC-800 was 53.38 emu g^{-1} and the obtained Co@NC-800 exhibited a hysteretic behavior, the coercivity was 49.65 Oe [43]. The inserted figure in Fig. 4b showed the Co@NC-800 could be attracted by the magnet, thus the magnetic Co@NC-800 showed great potential in removing pollutants from aqueous solution for its easy separation.

3.2. Catalytic performance

The catalytic activities of different systems towards TC degradation was exhibited in Fig. 5a. TC concentration after dark adsorption for 0.5 h was selected as the zero point (the adsorption of TC by samples was presented in Fig. S2). As presented in Fig. 5b, the TC solution was stable while noticeable TC removal was showed in PMS, NC-800/PMS and Co@NC-800/PMS systems due to the catalytic property of PMS. However, the Co@NC-800/PMS system exhibited the highest TC degradation rate with the kinetic constant of 0.7961 min^{-1}, which was 41 times higher than that of NC-800/PMS system (0.0196 min^{-1}). Therefore, Co nanoparticles inside the N-doped porous carbon played a vital role in TC removal activity. Moreover, the total organic carbon (TOC) removal efficiency of Co@NC-800/PMS system was as high as 74.7% (Fig. S4). After catalytic reaction, the Co leaching of Co@NC-800 was and 0.147 mg L^{-1}. Moreover, the water stability of the pristine and Co@NC-800 was tested by immersing 20 mg of catalyst in 100 mL water for 24 h. The Co leaching of ZIF-67 and Co@NC-800 were 3.524 mg L^{-1} and 0.021 mg L^{-1}, respectively. Therefore, the Co nanoparticles were well confined in carbon layers in Co@NC-800 with negligible Co leaching. Therefore, the Co nanoparticles were well confined in carbon layers in Co@NC-800 with negligible Co leaching.

3.3. Catalytic mechanism

Linear sweep voltammetry (LSV) was applied to estimate the electron-transfer process from the TC molecules to PMS on catalyst surface [44,45]. As showed in Fig. S5, there was no obvious current density in the presence of both TC solution and PMS when bare FTO acted as the working electrode. Moreover, a minor current density was showed in the copresence of PMS and TC when NC-800 was selected as a working electrode. Obviously, the current response increased remarkably in the electrolyte containing PMS and TC on the Co@NC-800 electrodes. The LSV results indicated that electron transfer on Co@NC-800 electrode interface was very fast compared to the pristine FTO electrode and NC-800 electrode. Moreover, the radical-trapping experiments were conducted and *tert*-butyl alcohol (TBA) as the trapping agent of $^{\cdot}OH$ radical, methanol as the trapping agent of $SO_4^{\cdot -}$ and $^{\cdot}OH$ radical, p-benzoquinone (BQ) as the trapping agent of $O_2^{\cdot -}$ radicals, NaN_3 as the trapping agent of $^1O_2$ [12,46]. As Fig. 6a and b showed, the TBA showed almost little impact on TC degradation while the removal efficiency reduced from 93.6% to 66.7% with MeOH added. Moreover, the removal efficiency significantly declined to 55.6% and 47.4% with BQ and NaN_3 added, respectively. Thus, the $O_2^{\cdot -}$ and $^1O_2$ were the dominating active species in TC degradation while $SO_4^{\cdot -}$ also involved in TC degradation in Co@NC-800/PMS system. Considering that $O_2^{\cdot -}$ radicals can be generated from the excited oxygen molecules, the contribution of $O_2^{\cdot -}$ radicals may be affected by the atmosphere environment [7]. By continuously injecting N_2 into the reaction system, the removal efficiency reduced from 93.6% to 78.4%, demonstrating that $O_2^{\cdot -}$ radicals involved in the catalytic reaction. Electron paramagnetic resonance (EPR) was further adopted by using 5,5-dimethyl-1-pyrroline N-oxide (DMPO) as the spin scavenger to confirm the presence of $O_2^{\cdot -}$ radicals and 2,2,6,6-tetramethyl-4-piperidinol (TMP) as the spin scavenger for $^1O_2$. The characteristic signals of DMPO-$O_2^{\cdot -}$ and TMP-$^1O_2$ were displayed in Co@NC-800/PMS system after reacted for 10 min, suggesting the formation of $O_2^{\cdot -}$ radicals and $^1O_2$ through PMS activation (Fig. 6c and d).

We had also investigated the XPS spectra of Co@NC-800 after the catalytic reaction (Fig. S6). The XPS survey spectra showed no noticeable change, indicating the Co@NC-800 catalyst was stable. Interestingly, the content of Co species and N species made a difference. The content of Co^{2+} species was increased from 36.2% to 45.8% after reaction while the Co^{3+} species decreased from 17.1% to 14.3% and the content of Co^0 decreased from 23.5% to 21.1%. During the catalytic reaction, the valence state of Co species changed significantly. The decrease of Co^{3+} species was due to the reaction of Co^{3+} and PMS to generate Co^{2+}, $SO_5^{\cdot -}$ and H^+ (Eq. (1)). Besides, the Co^{2+} can activate PMS to generate $SO_4^{\cdot -}$, Co^{3+} and OH^- (Eq. (2)). Because of the periodic cycle of Co^{2+}/Co^{3+}, the Co@NC-800/PMS system operated with high efficiency [15,47]. Moreover, the Co^0 not only can active PMS directly to produce $SO_4^{\cdot -}$ radicals and Co^{2+} (Eq. (3)) but also can react with Co^{3+} or O_2 to obtain Co^{2+} to ensure the sufficient Co^{2+} to

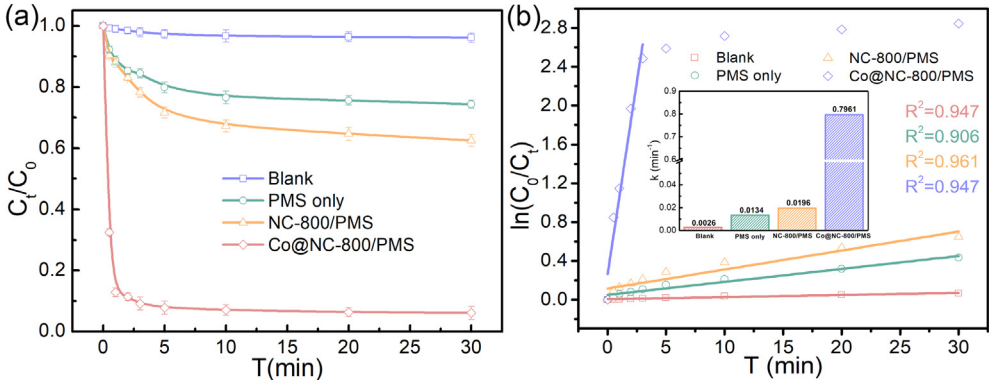

Fig. 5. (a) TC removal efficiencies under different systems (blank, PMS only, NC-800/PMS and Co@NC-800/PMS); (b) TC degradation kinetics under different system. The inserted figure in (b) exhibited the kinetic constant based on pseudo-first-order kinetic model and the different system (Experimental conditions: catalyst dosage = 0.2 g L^{-1}; initial TC concentration = 30 mg L^{-1}; PMS concentration = 0.2 g L^{-1}).

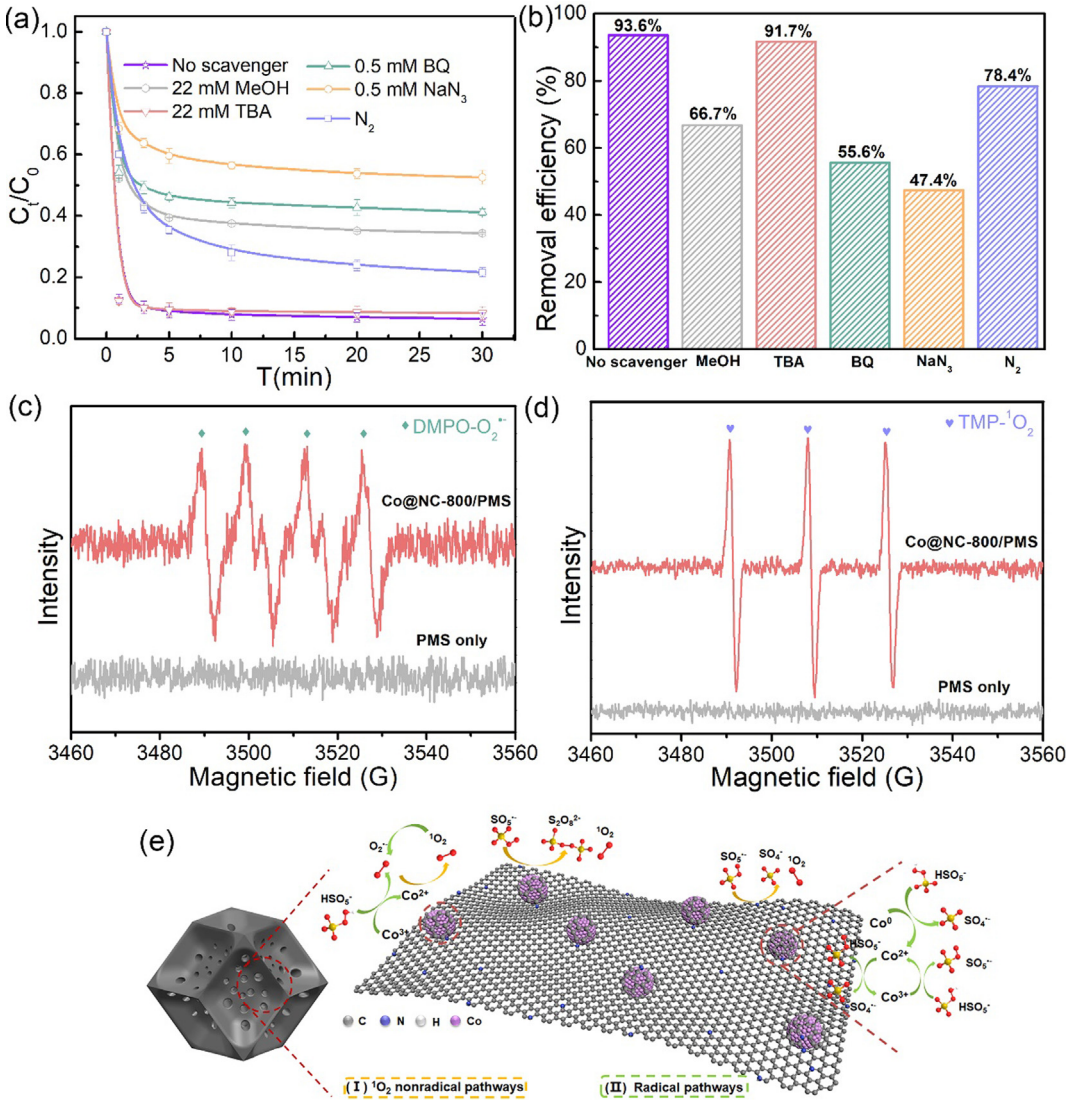

Fig. 6. TC removal efficiencies of Co@NC-800/PMS system with different radical scavengers (a) and (b); EPR spectra for Co@NC-800/PMS system in aqueous dispersion by spin trapping with DMPO (c) and TMP (d) at different time intervals (Experimental conditions: catalyst dosage = 0.2 g L^{-1}; initial TC concentration = 30 mg L^{-1}; PMS concentration = 0.2 g L^{-1}); (e) the proposed reaction mechanism of TC degradation by Co@NC-800/PMS system.

activate the PMS (Eqs. (4) and (5)). On the other hand, the content of pyridinic N increased from 43.2% to 65.8% and the graphitic N decreased from 35.6% to 19.1% after the catalytic reaction, suggesting the electron transfer may exist between N-Co and TC molecules [48]. Based on the trapping experiments, the $^1O_2$ and $O_2^{\cdot -}$ radicals were involved in the catalytic reaction. $O_2^{\cdot -}$ radicals can be obtained by the generation of H_2O_2 (Eq. (6)) and the reaction between H_2O_2 and Co^{3+} to produce $HO_2^{\cdot}$ (Eq. (7)) and the decomposition of $HO_2^{\cdot}$ to produce $O_2^{\cdot -}$ radicals (Eq. (8)) [49]. Moreover, the $O_2^{\cdot -}$ radicals could react with $HO_2^{\cdot}$ to produce $^1O_2$ and the self-reaction of $O_2^{\cdot -}$ radicals could regenerate H_2O_2 and $^1O_2$ (Eqs. (9) and (10)). The $^1O_2$ can be produced by the self-reaction of $SO_5^{\cdot -}$ (Eqs. (11) and (12)) for the high reaction rate ($\approx 2 \times 108$ m^{-1} S^{-1}) and low activation energy (7.4 ± 2.4 kcal mol^{-1}) [50].

Based on the above deduction, non-radical ($^1O_2$) and radical ($SO_4^{\cdot -}$ and $O_2^{\cdot -}$) processes were included in TC degradation by Co@NC-800/PMS system (the proposed reaction mechanism was showed in Fig. 6e). The porous N-doped carbon skeleton with high porosity and surface area not only attributed to the uniform distribution of Co nanoparticles but also promoted the adsorption of TC molecules and the electron transfer between Co@NC-800 and TC molecules [39]. The Co nanoparticles were confined within the carbon, which was vital for the stability of catalyst [18]. The electron transfer between N and Co species made the Co@NC-800/PMS system operated efficiently. Moreover, the magnetic Co^0 made the Co@NC-800 be separated with high efficiency. Therefore, the Co@NC-800 showed a superb activity in the activation of PMS for TC degradation.

$$Co^{3+} + HSO_5^- \rightarrow SO_5^{\cdot -} + Co^{2+} + H^+ \quad (1)$$

$$Co^{2+} + HSO_5^- \rightarrow SO_4^{\cdot -} + Co^{3+} + OH^- \quad (2)$$

$$Co^0 + 2HSO_5^- \rightarrow 2SO_4^{\cdot -} + Co^{2+} + 2OH^- \quad (3)$$

$$2Co^0 + 2H_2O + O_2 \rightarrow 2Co^{2+} + 4OH^- \quad (4)$$

$$Co^0 + 2Co^{3+} \rightarrow 3Co^{2+} \quad (5)$$

$$HSO_5^- + H_2O \rightarrow H_2O_2 + HSO_4^- \quad (6)$$

$$Co^{3+} + H_2O_2 \rightarrow Co^{2+} + HO_2^{\cdot} + H^+ \quad (7)$$

$$HO_2^{\cdot} \rightarrow O_2^{\cdot -} + H^+ \quad (8)$$

$$O_2^{\cdot -} + HO_2^{\cdot} \rightarrow HO_2^- + {}^1O_2 \quad (9)$$

$$2O_2^{\cdot -} + H^+ \rightarrow H_2O_2 + {}^1O_2 \quad (10)$$

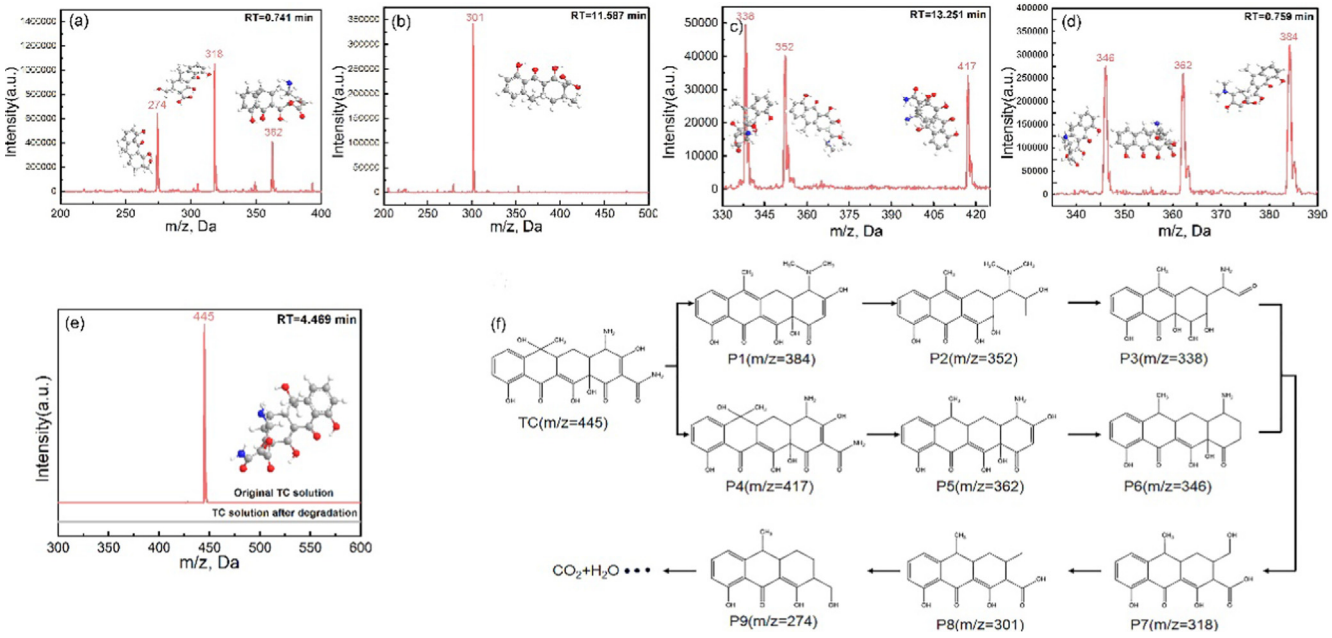

Fig. 7. LC-MS analysis of TC intermediates in the degradation reaction with Co@NC-800/PMS (a-e); the proposed transformation pathways of TC degradation (f).

$$SO_5^{\cdot -} + SO_5^{\cdot -} \rightarrow S_2O_8^{2-} + {}^1O_2 \quad (11)$$

$$SO_5^{\cdot -} + SO_5^{\cdot -} \rightarrow 2SO_4^{\cdot -} + {}^1O_2 \quad (12)$$

3.4. TC degradation pathway

Based on the catalytic mechanism, the active species ($SO_4^{\cdot -}$, $O_2^{\cdot -}$ and $^1O_2$) produced by Co@NC-800/PMS system can attack the TC molecules and generate low molecular weight products. As showed in Fig. 7e, the peak at the retention time of 4.469 min was corresponded to the TC molecules (the analysis of TC intermediates was showed in the Supporting Information). Compared to the original TC solution, the peak intensity of TC molecules in TC solution after reaction reduced remarkably, suggesting the high degradation efficiency of Co@NC-800/PMS system. Fig. 7a–d showed the degradation products and their possible molecule structures. The proposed transformation pathway was presented in Fig. 7f. It was obvious that the TC molecules was oxidized and finally transformed to CO_2 and H_2O. The TOC removal efficiency was as high as 74.67%, indicating the superiority of both the radical and non-radical pathway in Co@NC-800/PMS system.

3.5. Effects of experimental conditions on catalytic performance

The versatility of Co@NC-800/PMS system under various conditions was of great importance. The removal efficiency could be improved by increasing PMS concentration (Fig. 8a) and reaction temperature (Fig. 8d). The TC concentration had negative effect on removal efficiency while the removal efficiency of 85.8% was obtained as the TC concentration was 50 mg L^{-1} (Fig. 8b). Anyhow, high removal efficiency in low TC concentration was beneficial for actual wastewater treatment. Solution pH value had an effect on the removal efficiency of Co@NC-800/PMS system (Fig. 8c). In the pH value range of 4–10, high removal efficiency (more than 90%) could be obtained, while the removal efficiency of pH 2 and pH 12 were 85.4% and 68.9%, respectively. The point of zero charge (pH_{pzc}) of Co@NC-800 was calculated to be 8.13 (Fig. S7), thus the TC molecules and Co@NC-800 with the same charge when the pH value was 2 and 12, the electrostatic repulsion between Co@NC-800 and TC molecules resulted in the low removal efficiency. In addition, the HSO_5^- was mainly in the form of H_2SO_5 at pH 2, which limited the decompose of HSO_5^- [51]. When the pH value was 12, the $Co(OH)_2$ might formed and reduced the catalytic performance [52]. Thus, the Co@NC-800/PMS system performed excellent degradation efficiency towards TC in a wide pH range of 4–10.

Moreover, the common inorganic species (like Cl^-, SO_4^{2-}, and PO_4^{3-} ions) with various concentrations had a negative effect on TC degradation (Fig. S8a–c). The Cl^-, SO_4^{2-}, and PO_4^{3-} ions can quench the $SO_4^{\cdot -}$ and $^{\cdot}OH$ radicals [53]. Obviously, compared to Cl^-, SO_4^{2-} ions, PO_4^{3-} ions had the greatest effect on degradation efficiency. PO_4^{3-} ions not only trapped the radicals but also chelated with Co [54]. In addition, humic acid with various concentrations had little impact on TC degradation (Fig. S8d). The catalytic performance of Co@NC-800/PMS system was evaluated in multiple antibiotics degradation (Fig. 9a), such as TC, OTC (oxytetracycline), CTC (chlortetracycline) and DOX (deoxytetracycline). The high removal efficiency of Co@NC-800/PMS system could be obtained (more than 90%). Surprisingly, high TC removal efficiencies of 93.6%, 91.3%, 91.7% were obtained by Co@NC-800/PMS system in pharmaceutical wastewater, river water and tap water (Fig. 9b, the water quality parameters were listed in Table S1). In a word, the Co@NC-800 system exhibited high removal efficiency towards multiple antibiotics and suffered less interference from solution pH value, the co-existing inorganic ions and organic matters, suggesting a great potential in various water bodies for the combined action of non-radical and radical pathways.

3.6. Comparation of homogeneous catalytic system and stability tests

The Co@NC-800/PMS system was compared with homogeneous Co^{2+}/PMS system. Fig. 10a showed the removal efficiency of 68.1% was obtained by the homogeneous Co^{2+}/PMS system in 30 min, while the TC removal efficiency of 91.2% could be obtained by Co@NC-800/PMS system within 5 min. The experimental results highlighted the high degradation efficiency of the Co@NC-800/PMS system. In addition, compared to the homogeneous system, the Co@NC-800/PMS system exhibited excellent recyclability. The Co@NC-800 catalyst after reaction was collected by an external magnet and ultrasonically washed in water and vacuum dried for further use. After reused for 4 times, the removal efficiency of Co@NC-800 was almost no declined (Fig. 10b), suggesting the Co@NC-800 catalyst possessed great recyclability and the Co@NC-800/PMS system had great potential for wastewater remediation.

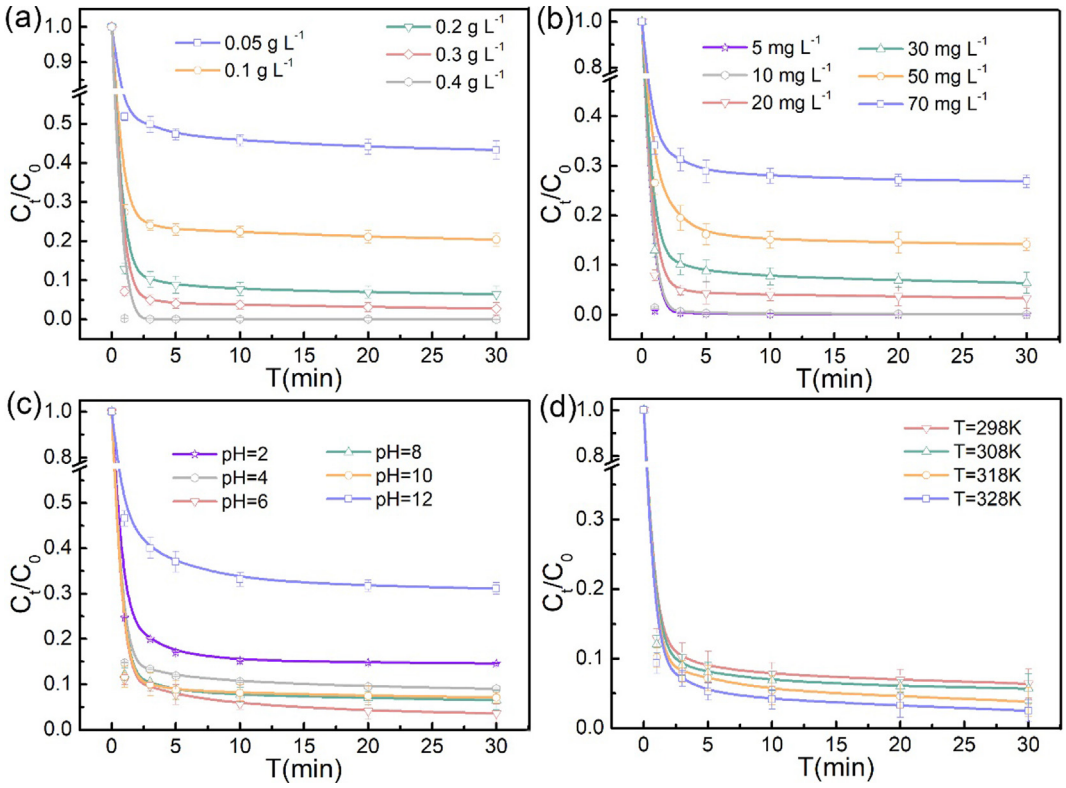

Fig. 8. (a) Effects of PMS dosage (Experimental conditions: catalyst dosage = 0.2 g L^{-1}, initial TC concentration = 30 mg L^{-1}); (b) TC concentration (Experimental conditions: catalyst dosage = 0.2 g L^{-1}; PMS concentration = 0.2 g L^{-1}); (c) solution pH value (Experimental conditions: catalyst dosage = 0.2 g L^{-1}; initial TC concentration = 30 mg L^{-1}; PMS concentration = 0.2 g L^{-1}) and (d) temperature (Experimental conditions: catalyst dosage = 0.2 g L^{-1}; initial TC concentration = 30 mg L^{-1}; PMS concentration = 0.2 g L^{-1}) on TC degradation by Co@NC-800/PMS system.

4. Conclusion

In this study, ZIF-67 was applied as a self-sacrificing template to fabricate Co@NC-800 through a two-step pyrolysis process. Characterization results showed that the obtained Co@NC-800 inherited rhombic dodecahedron morphology, the Co nanoparticles formed in the pyrolysis process and confined within the N-doped porous carbon. Moreover, the porous structure of Co@NC-800 was conductive to pollutants diffusion and active sites exposition, which was attributed to PMS activation by Co nanoparticles. The TC degradation kinetics of Co@NC-800/PMS was 41 times faster than NC-800/PMS. Moreover, the Co@NC-800/PMS system suffered less interference from co-existing anions/organic matters in water and showed high efficiency in a wide pH range of 4–10. More importantly, Co@NC-800/PMS system showed high degradation efficiency towards multiple antibiotics and displayed high TC removal rate in various water bodies. Trapping experiments showed the $SO_4^{\cdot -}$, $O_2^{\cdot -}$ and $^1O_2$ were involved in PMS activation and both the radical and non-radical pathways in Co@NC-800/PMS system presented superiority in TC degradation. The porous N-doped carbon skeleton promoted the adsorption of TC molecules and the electron transfer between Co@NC-800 and TC molecules. The Co nanoparticles were well confined and no obvious Co leaching after catalytic reaction, which was vital for the stability of catalyst. Moreover, the existence of magnetic Co^0 made the Co@NC-800 be separated with high efficiency. Therefore, this work provided a design of PMS catalyst using confinement for TC-containing wastewater remediation and also proposed a radical and non-radical pathway with high efficiency to understand the mechanism of the PMS activation reaction.

CRediT authorship contribution statement

Jiao Cao: Data curation and Writing - original draft. **Zhaohui Yang:** Supervision and Funding acquisition. **Weiping Xiong:** Writing-reviewing and editing. **Yaoyu Zhou:** Experimental operation. **You Wu:**

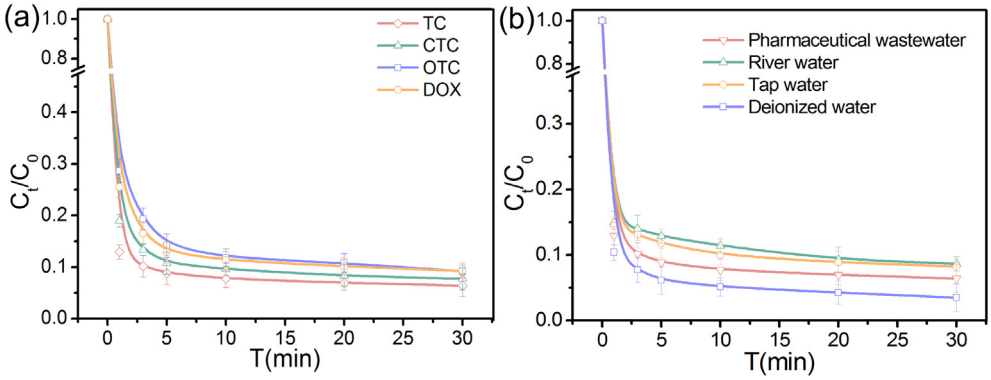

Fig. 9. (a) Catalytic elimination of organic pollutants on Co@NC-800/PMS system (Experimental conditions: catalyst dosage = 0.2 g L^{-1}; initial TC concentration = 30 mg L^{-1}; initial CTC concentration = 30 mg L^{-1}; initial OTC concentration = 30 mg L^{-1}; initial DOX concentration = 30 mg L^{-1}; PMS concentration = 0.2 g L^{-1}). (b) TC degradation by Co@NC-800/PMS system in real samples (Experimental conditions: catalyst dosage = 0.2 g L^{-1}; initial TC concentration = 30 mg L^{-1}; PMS concentration = 0.2 g L^{-1}).

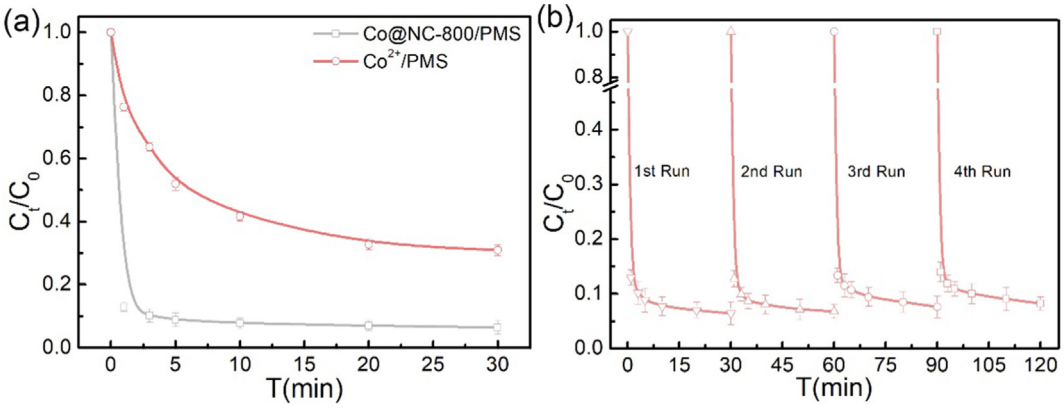

Fig. 10. (a) TC degradation in homogeneous catalysis system; (b) recycling tests of Co@NC-800 in decomposition of PMS for TC degradation (Experiment condition: catalyst dosage = 0.2 g L^{-1}; $CoCl_2$ dosage = 0.2 g L^{-1}; initial TC concentration = 30 mg L^{-1}; PMS concentration = 0.2 g L^{-1}).

Investigation and Validation. **Meiying Jia:** Writing-reviewing and editing. **Saiwu Sun:** Resources and Visualization. **Chengyun Zhou:** Writing - review & editing. **Yanru Zhang:** Writing - review & editing. **Renhua Zhong:** Writing - review & editing.

Declaration of Competing Interest

The authors declare that they have no known competing financial interests or personal relationships that could have appeared to influence the work reported in this paper.

Acknowledgements

The study was financially supported by the National Natural Science Foundation of China (51578223, 51521006 and 51709103).

Appendix A. Supplementary material

Supplementary data to this article can be found online at https://doi.org/10.1016/j.seppur.2020.117237.

References

[1] J. Cao, Z.H. Yang, W.P. Xiong, Y.Y. Zhou, Y.R. Peng, X. Li, C.Y. Zhou, R. Xu, One-step synthesis of Co-doped UiO-66 nanoparticle with enhanced removal efficiency of tetracycline: Simultaneous adsorption and photocatalysis, Chem. Eng. J. 353 (2018) 126–137.
[2] Z.H. Yang, J. Cao, Y.P. Chen, X. Li, W.P. Xiong, Y.Y. Zhou, C.Y. Zhou, R. Xu, Mn-doped zirconium metal-organic framework as an effective adsorbent for removal of tetracycline and Cr(VI) from aqueous solution, Micropor. Mesopor. Mater. 277 (2019) 277–285.
[3] C. Zhou, P. Xu, C. Lai, C. Zhang, G. Zeng, D. Huang, M. Cheng, L. Hu, W. Xiong, X. Wen, L. Qin, J. Yuan, W. Wang, Rational design of graphic carbon nitride co-polymers by molecular doping for visible-light-driven degradation of aqueous sulfamethazine and hydrogen evolution, Chem. Eng. J. 359 (2019) 186–196.
[4] W. Wang, Z. Zeng, G. Zeng, C. Zhang, R. Xiao, C. Zhou, W. Xiong, Y. Yang, L. Lei, Y. Liu, D. Huang, M. Cheng, Y. Yang, Y. Fu, H. Luo, Y. Zhou, Sulfur doped carbon quantum dots loaded hollow tubular g-C_3N_4 as novel photocatalyst for destruction of Escherichia coli and tetracycline degradation under visible light, Chem. Eng. J. 378 (2019) 122132.
[5] C. Feng, L. Tang, Y. Deng, G. Zeng, J. Wang, Y. Liu, Z. Chen, J. Yu, J. Wang, Enhancing optical absorption and charge transfer: Synthesis of S-doped h-BN with tunable band structures for metal-free visible-light-driven photocatalysis, Appl. Catal. B 256 (2019) 117827.
[6] H. Wang, J. Zhang, X. Yuan, L. Jiang, Q. Xia, H. Chen, Photocatalytic removal of antibiotics from natural water matrices and swine wastewater via Cu(I) coordinately polymeric carbon nitride framework, Chem. Eng. J. 392 (2020) 123638.
[7] J. Yu, L. Tang, Y. Pang, G. Zeng, H. Feng, J. Zou, J. Wang, C. Feng, X. Zhu, X. Ouyang, J. Tan, Hierarchical porous biochar from shrimp shell for persulfate activation: A two-electron transfer path and key impact factors, Appl. Catal. B 260 (2020) 118160.
[8] J. Kang, L. Zhou, X. Duan, H. Sun, Z. Ao, S. Wang, Degradation of cosmetic microplastics via functionalized carbon nanosprings, Matter (2019).
[9] C. Wang, J. Kang, P. Liang, H. Zhang, H. Sun, M.O. Tadé, S. Wang, Ferric carbide nanocrystals encapsulated in nitrogen-doped carbon nanotubes as an outstanding environmental catalyst, Environ. Sci. Nano 4 (2017) 170–179.
[10] G. Liao, Y. Gong, L. Zhang, H. Gao, G.-J. Yang, B. Fang, Semiconductor polymeric graphitic carbon nitride photocatalysts: the "holy grail" for the photocatalytic hydrogen evolution reaction under visible light, Energy Environ. Sci. 12 (2019) 2080–2147.
[11] Y. Lin, H. Liu, C. Yang, X. Wu, C. Du, L. Jiang, Y. Zhong, Gama-graphyne as photogenerated electrons transfer layer enhances photocatalytic performance of silver phosphate, Appl. Catal. B 264 (2020) 118479.
[12] L. Xie, Z. Yang, W. Xiong, Y. Zhou, J. Cao, Y. Peng, X. Li, C. Zhou, R. Xu, Y. Zhang, Construction of MIL-53(Fe) metal-organic framework modified by silver phosphate nanoparticles as a novel Z-scheme photocatalyst: Visible-light photocatalytic performance and mechanism investigation, Appl. Surf. Sci. 465 (2019) 103–115.
[13] P. Shao, J. Tian, F. Yang, X. Duan, S. Gao, W. Shi, X. Luo, F. Cui, S. Luo, S. Wang, Identification and regulation of active sites on nanodiamonds: establishing a highly efficient catalytic system for oxidation of organic contaminants, Adv. Funct. Mater. 28 (2018) 1705295.
[14] T. Liu, D. Zhang, K. Yin, C. Yang, S. Luo, J.C. Crittenden, Degradation of thiacloprid via unactivated peroxymonosulfate: The overlooked singlet oxygen oxidation, Chem. Eng. J. 388 (2020) 124264.
[15] G.P. Anipsitakis, D.D. Dionysiou, Degradation of organic contaminants in water with sulfate radicals generated by the conjunction of peroxymonosulfate with cobalt, Environ. Sci. Technol. 37 (2003) 4790–4797.
[16] R. Xiao, Z. Luo, Z. Wei, S. Luo, R. Spinney, W. Yang, D.D. Dionysiou, Activation of peroxymonosulfate/persulfate by nanomaterials for sulfate radical-based advanced oxidation technologies, Curr. Opin. Chem. Eng. 19 (2018) 51–58.
[17] Z. Chen, R. Wu, Y. Liu, Y. Ha, Y. Guo, D. Sun, M. Liu, F. Fang, Ultrafine Co nanoparticles encapsulated in carbon-nanotubes-grafted graphene sheets as advanced electrocatalysts for the hydrogen evolution reaction, Adv. Mater. 30 (2018) 1802011.
[18] Z. Yang, J. Qian, A. Yu, B. Pan, Singlet oxygen mediated iron-based Fenton-like catalysis under nanoconfinement, Proc. Natl. Acad. Sci. 116 (2019) 6659–6664.
[19] J. Jin, Z. Yang, W. Xiong, Y. Zhou, R. Xu, Y. Zhang, J. Cao, X. Li, C. Zhou, Cu and Co nanoparticles co-doped MIL-101 as a novel adsorbent for efficient removal of tetracycline from aqueous solutions, Sci. Total Environ. 650 (2019) 408–418.
[20] C.-Y. Su, H. Cheng, W. Li, Z.-Q. Liu, N. Li, Z. Hou, F.-Q. Bai, H.-X. Zhang, T.-Y. Ma, Atomic modulation of FeCo–nitrogen–carbon bifunctional oxygen electrodes for rechargeable and flexible all-solid-state zinc-air battery, Adv. Energy Mater. 7 (2017) 1602420.
[21] Q. Wang, K. Ye, L. Xu, W. Hu, Y. Lei, Y. Zhang, Y. Chen, K. Zhou, J. Jiang, J.M. Basset, D. Wang, Y. Li, Carbon nanotube-encapsulated cobalt for oxygen reduction: integration of space confinement and N-doping, Chem. Commun. 55 (2019) 14801–14804.
[22] T.W. van Deelen, C. Hernández Mejía, K.P. de Jong, Control of metal-support interactions in heterogeneous catalysts to enhance activity and selectivity, Nat. Cataly. 2 (2019) 955–970.
[23] G. Pacchioni, H.-J. Freund, Controlling the charge state of supported nanoparticles in catalysis: lessons from model systems, Chem. Soc. Rev. 47 (2018) 8474–8502.
[24] Z. Liang, C. Qu, D. Xia, R. Zou, Q. Xu, Atomically dispersed metal sites in MOF-based materials for electrocatalytic and photocatalytic energy conversion, Angew. Chem. Int. Ed. 57 (2018) 9604–9633.
[25] N.L. Torad, R.R. Salunkhe, Y. Li, H. Hamoudi, M. Imura, Y. Sakka, C.-C. Hu, Y. Yamauchi, Electric double-layer capacitors based on highly graphitized nanoporous carbons derived from ZIF-67, Chem. – Europ. J. 20 (2014) 7895–7900.
[26] K.-Y.A. Lin, B.-J. Chen, Prussian blue analogue derived magnetic carbon/cobalt/iron nanocomposite as an efficient and recyclable catalyst for activation of peroxymonosulfate, Chemosphere 166 (2017) 146–156.
[27] Y. Tu, P. Ren, D. Deng, X. Bao, Structural and electronic optimization of graphene encapsulating binary metal for highly efficient water oxidation, Nano Energy 52 (2018) 494–500.
[28] T. Zeng, M. Yu, H. Zhang, Z. He, J. Chen, S. Song, Fe/Fe_3C@N-doped porous carbon hybrids derived from nano-scale MOFs: robust and enhanced heterogeneous catalyst for peroxymonosulfate activation, Catal. Sci. Technol. 7 (2017) 396–404.

[29] M. Li, J. Meng, Q. Li, M. Huang, X. Liu, K.A. Owusu, Z. Liu, L. Mai, Finely crafted 3D electrodes for dendrite-free and high-performance flexible fiber-shaped Zn–Co batteries, Adv. Funct. Mater. 28 (2018) 1802016.
[30] S. An, G. Zhang, T. Wang, W. Zhang, K. Li, C. Song, J.T. Miller, S. Miao, J. Wang, X. Guo, High-density ultra-small clusters and single-atom Fe sites embedded in graphitic carbon nitride (g-C_3N_4) for highly efficient catalytic advanced oxidation processes, ACS Nano 12 (2018) 9441–9450.
[31] B.Y. Xia, Y. Yan, N. Li, H.B. Wu, X.W. Lou, X. Wang, A metal–organic framework-derived bifunctional oxygen electrocatalyst, Nat. Energy 1 (2016) 15006.
[32] R. Banerjee, A. Phan, B. Wang, C. Knobler, H. Furukawa, M. O'Keeffe, O.M. Yaghi, High-throughput synthesis of zeolitic imidazolate frameworks and application to CO_2 capture, Science (New York, N.Y.) 319 (2008) 939–943.
[33] J. Li, H. Wang, X. Yuan, J. Zhang, J.W. Chew, Metal-organic framework membranes for wastewater treatment and water regeneration, Coord. Chem. Rev. 404 (2020) 213116.
[34] Q. Xia, H. Wang, B. Huang, X. Yuan, J. Zhang, J. Zhang, L. Jiang, T. Xiong, G. Zeng, State-of-the-art advances and challenges of iron-based metal organic frameworks from attractive features, synthesis to multifunctional applications, Small 15 (2019) 1803088.
[35] X. Ma, Y.-X. Zhou, H. Liu, Y. Li, H.-L. Jiang, A MOF-derived Co–CoO@N-doped porous carbon for efficient tandem catalysis: dehydrogenation of ammonia borane and hydrogenation of nitro compounds, Chem. Commun. 52 (2016) 7719–7722.
[36] X. Wang, W. Zhong, Y. Li, Nanoscale Co-based catalysts for low-temperature CO oxidation, Catal. Sci. Technol. 5 (2015) 1014–1020.
[37] Y. Yu, S. You, J. Du, Z. Xing, Y. Dai, H. Chen, Z. Cai, N. Ren, J. Zou, ZIF-67-derived CoO (tetrahedral Co^{2+})@nitrogen-doped porous carbon protected by oxygen vacancies-enriched SnO_2 as highly active catalyst for oxygen reduction and Pt co-catalyst for methanol oxidation, Appl. Catal. B 259 (2019) 118043.
[38] C. Yan, G. Chen, X. Zhou, J. Sun, C. Lv, Template-based engineering of carbon-doped Co_3O_4 hollow nanofibers as anode materials for lithium-ion batteries, Adv. Funct. Mater. 26 (2016) 1428–1436.
[39] H. Chu, D. Zhang, B. Jin, M. Yang, Impact of morphology on the oxygen evolution reaction of 3D hollow Cobalt-Molybdenum Nitride, Appl. Catal. B 255 (2019) 117744.
[40] J. Tian, Q. Liu, A.M. Asiri, X. Sun, Self-supported nanoporous cobalt phosphide nanowire arrays: an efficient 3D hydrogen-evolving cathode over the wide range of pH 0–14, J. Am. Chem. Soc. 136 (2014) 7587–7590.
[41] W. Ma, N. Wang, Y. Fan, T. Tong, X. Han, Y. Du, Non-radical-dominated catalytic degradation of bisphenol A by ZIF-67 derived nitrogen-doped carbon nanotubes frameworks in the presence of peroxymonosulfate, Chem. Eng. J. 336 (2018) 721–731.
[42] Y. Pan, K. Sun, S. Liu, X. Cao, K. Wu, W.-C. Cheong, Z. Chen, Y. Wang, Y. Li, Y. Liu, D. Wang, Q. Peng, C. Chen, Y. Li, Core-shell ZIF-8@ZIF-67-derived CoP nanoparticle-embedded N-doped carbon nanotube hollow polyhedron for efficient overall water splitting, J. Am. Chem. Soc. 140 (2018) 2610–2618.
[43] W. Xiong, Z. Zeng, G. Zeng, Z. Yang, R. Xiao, X. Li, J. Cao, C. Zhou, H. Chen, M. Jia, Y. Yang, W. Wang, X. Tang, Metal-organic frameworks derived magnetic carbon-αFe/Fe_3C composites as a highly effective adsorbent for tetracycline removal from aqueous solution, Chem. Eng. J. 374 (2019) 91–99.
[44] L. Tang, Y. Liu, J. Wang, G. Zeng, Y. Deng, H. Dong, H. Feng, J. Wang, B. Peng, Enhanced activation process of persulfate by mesoporous carbon for degradation of aqueous organic pollutants: Electron transfer mechanism, Appl. Catal. B 231 (2018) 1–10.
[45] H. Lee, H.-I. Kim, S. Weon, W. Choi, Y.S. Hwang, J. Seo, C. Lee, J.-H. Kim, Activation of persulfates by graphitized nanodiamonds for removal of organic compounds, Environ. Sci. Technol. 50 (2016) 10134–10142.
[46] S. Dhaka, R. Kumar, S.-H. Lee, M.B. Kurade, B.-H. Jeon, Degradation of ethyl paraben in aqueous medium using advanced oxidation processes: Efficiency evaluation of UV-C supported oxidants, J. Cleaner Prod. 180 (2018) 505–513.
[47] Y. Wang, S. Zhao, W. Fan, Y. Tian, X. Zhao, The synthesis of novel Co–Al_2O_3 nanofibrous membranes with efficient activation of peroxymonosulfate for bisphenol A degradation, Environ. Sci. Nano 5 (2018) 1933–1942.
[48] L. Lyu, D. Yan, G. Yu, W. Cao, C. Hu, Efficient destruction of pollutants in water by a dual-reaction-center fenton-like process over carbon nitride compounds-complexed Cu(II)-$CuAlO_2$, Environ. Sci. Technol. 52 (2018) 4294–4304.
[49] C. Liu, L. Liu, X. Tian, Y. Wang, R. Li, Y. Zhang, Z. Song, B. Xu, W. Chu, F. Qi, A. Ikhlaq, Coupling metal–organic frameworks and g-C_3N_4 to derive Fe@N-doped graphene-like carbon for peroxymonosulfate activation: Upgrading framework stability and performance, Appl. Catal. B 255 (2019) 117763.
[50] J. Cao, S. Sun, X. Li, Z. Yang, W. Xiong, Y. Wu, M. Jia, Y. Zhou, C. Zhou, Y. Zhang, Efficient charge transfer in aluminum-cobalt layered double hydroxide derived from Co-ZIF for enhanced catalytic degradation of tetracycline through peroxymonosulfate activation, Chem. Eng. J. 122802 (2019).
[51] K.H. Chan, W. Chu, Degradation of atrazine by cobalt-mediated activation of peroxymonosulfate: Different cobalt counteranions in homogenous process and cobalt oxide catalysts in photolytic heterogeneous process, Water Res. 43 (2009) 2513–2521.
[52] Y. Ren, L. Lin, J. Ma, J. Yang, J. Feng, Z. Fan, Sulfate radicals induced from peroxymonosulfate by magnetic ferrospinel MFe_2O_4 (M = Co, Cu, Mn, and Zn) as heterogeneous catalysts in the water, Appl. Catal. B 165 (2015) 572–578.
[53] Y. Ji, L. Wang, M. Jiang, J. Lu, C. Ferronato, J.-M. Chovelon, The role of nitrite in sulfate radical-based degradation of phenolic compounds: An unexpected nitration process relevant to groundwater remediation by in-situ chemical oxidation (ISCO), Water Res. 123 (2017) 249–257.
[54] F. Qi, W. Chu, B. Xu, Modeling the heterogeneous peroxymonosulfate/Co-MCM41 process for the degradation of caffeine and the study of influence of cobalt sources, Chem. Eng. J. 235 (2014) 10–18.